Monthly Notices of the ROYAL ASTRONOMICAL SOCIETY

MNRAS **547,** 1–12 (2026) https://doi.org/10.1093/mnras/stag473
Advance Access publication 2026 March 10

MIGHTEE/COSMOS-3D: the discovery of three spectroscopically confirmed radio-selected star-forming galaxies at $z = 4.9$–5.6

R. G. Varadaraj [1★] A. Saxena [1,2] S. Fakiolas,[1] I. H. Whittam [1,3] M. J. Jarvis [1,3] R. A. Meyer [4] C. L. Hale,[1,5] K. Kakiichi,[6,7] M. Li,[8] J. B. Champagne [9] B. Jin [10] Z. J. Li[11,12] and M. Shuntov[6,7]

[1]*Astrophysics, Department of Physics, University of Oxford, Keble Road, Oxford OX1 3RH, UK*
[2]*Department of Physics and Astronomy, University College London, Gower Street, London WC1E 6BT, UK*
[3]*Department of Physics and Astronomy, University of the Western Cape, Robert Sobukwe Road, 7535 Bellville, Cape Town, South Africa*
[4]*Department of Astronomy, University of Geneva, Chemin Pegasi 51, CH-1290 Versoix, Switzerland*
[5]*Institute for Astronomy, University of Edinburgh, Royal Observatory Edinburgh, Blackford Hill, Edinburgh EH9 3HJ, UK*
[6]*Cosmic Dawn Center (DAWN), Denmark*
[7]*Niels Bohr Institute, University of Copenhagen, Jagtvej 128, DK-2200 Copenhagen, Denmark*
[8]*Department of Astronomy, Tsinghua University, Beijing 100084, China*
[9]*Steward Observatory, University of Arizona, 933 N Cherry Ave, Tucson, AZ 85721, USA*
[10]*Department of Astronomy, University of Michigan, 1085 S. University Ave., Ann Arbor, MI 48109, USA*
[11]*Chinese Academy of Sciences South America Center for Astronomy (CASSACA), National Astronomical Observatories of China (NAOC), CAS, 20A Datun Road, Beijing 100012, China*
[12]*School of Astronomy and Space Sciences, University of Chinese Academy of Sciences, Beijing 100049, China*

Accepted 2026 February 27. in original form 2026 February 5

ABSTRACT

Radio observations offer a dust-independent probe of star formation and active galactic nucleus (AGN) activity, but sufficiently deep data are required to access the cross-over luminosity between these processes at high redshift ($z > 4.5$). We present three spectroscopically confirmed high-redshift radio sources (HzRSs) detected at 1.3 GHz at $z = 4.9$–5.6, with radio luminosities spanning $L_{1.3\,\mathrm{GHz}} \approx 2$–$5 \times 10^{24}\,\mathrm{W\,Hz^{-1}}$. These sources were first identified as high-redshift candidates through spectral energy distribution (SED) fitting of archival *Hubble*, *James Webb Space Telescope* (*JWST*) NIRCam + MIRI, and ground-based photometry, and then spectroscopically confirmed via the H α emission line using wide-field slitless spectroscopy from *JWST* COSMOS-3D. The star formation rates (SFRs) measured from SED fitting, the H α flux, and the 1.3 GHz luminosity, span $\sim$ 100–1800 $\mathrm{M_\odot\,yr^{-1}}$, demonstrating broad agreement between these SFR tracers. We find that these three sources lie either on or 0.5–1.0 dex above the star-forming main sequence at $z = 4$–6 and have undergone a recent burst of star formation. The sources have extended rest-ultraviolet (UV)/optical morphologies with no evidence for a dominant point source component, indicating that an AGN is unlikely to dominate their rest-UV and optical emission. Two of the sources have complex, multicomponent rest-frame UV/optical morphologies, suggesting that their starbursts may be triggered by merging activity. These HzRSs open up a new window towards probing radio emission powered by star formation alone at $z > 4.5$, representing a remarkable opportunity to begin tracing star formation, independent of dust, in the early Universe.

Key words: galaxies: evolution – galaxies: high-redshift – radio continuum: galaxies.

1 INTRODUCTION

High-redshift ($z > 4.5$) radio sources (HzRSs) provide an unparalleled dust-free window into the physics of galaxies in the early Universe. Their radio activity originates from synchrotron radiation produced either by the release of energy by accreting supermassive black holes (SMBHs) in active galactic nuclei (AGNs), or by short-lived massive stars that emit cosmic rays when turning supernova, providing a tracer of the star-formation rate. This means HzRSs are ideal laboratories for studying the physical mechanisms governing the growth and eventual quenching of high-redshift galaxies, such as gas accretion, black hole growth, and feedback processes impacting the interstellar medium. Powerful HzRSs are also often seen at the centres of massive protoclusters, with a number of star-forming galaxies with strong Lyα and H α emission seen in their environments (e.g. B. P. Venemans et al. 2007; G. Miley & C. De Breuck 2008; S. I. Muldrew, N. A. Hatch & E. A. Cooke 2015; R. A. Overzier 2016). Most HzRSs discovered to date are classified as 'radio-loud' AGNs with radio flux densities only achieved by luminous jets and lobes produced by the accretion of material onto a central SMBH (C. G. Bornancini

★ E-mail: rohan.varadaraj@physics.ox.ac.uk

© The Author(s) 2026.
Published by Oxford University Press on behalf of Royal Astronomical Society. This is an Open Access article distributed under the terms of the Creative Commons Attribution License (https://creativecommons.org/licenses/by/4.0/), which permits unrestricted reuse, distribution, and reproduction in any medium, provided the original work is properly cited.

et al. 2007; J. J. Bryant et al. 2009; M. J. Jarvis et al. 2009; A. Saxena et al. 2018b; A. Capetti et al. 2025). However, below a luminosity of roughly $L_{1.3\,\mathrm{GHz}} \sim 10^{24}\,\mathrm{W\,Hz^{-1}}$, the radio emission can arise either from AGN jets with lower powers than those in previous studies, or by intense star formation (SF; e.g. J. J. Condon 1992; E. M. Sadler et al. 2002; T. Mauch & E. M. Sadler 2007; M. Novak et al. 2017; N. J. Thykkathu et al. 2026). This regime is largely unexplored by searches for HzRSs, due to the depth of the radio continuum data that is required to detect such sources at high redshift. Both of these classes of HzRSs are interesting and can provide vital insights into rare sources at these redshifts; we are either detecting the most extreme starbursts at high redshifts (SFR $\sim 10^2$–$10^3\,\mathrm{M_\odot\,yr^{-1}}$) if all the radio emission is due to SF (e.g. H. S. B. Algera et al. 2020; J. A. Zavala et al. 2023), or a population of lower-powered radio jets which have not previously been studied at these redshifts, which could be responsible for shutting down SF at such early epochs (e.g. Y. Dubois et al. 2013). In the former case, the radio detections of these extreme starbursts will allow us to measure their SFRs unbiased by dust obscuration. Moreover, radio observations provide an efficient method of identifying these rare objects due to the combination of areal coverage and depth, compared to Atacama Large Millimeter Array (ALMA) which is limited to narrow fields (e.g. M. Franco et al. 2018), and far-infrared observations (e.g. Submillimetre Common-User Bolometer Array (SCUBA); Herschel, I. Smail et al. 2002; A. Lapi et al. 2011) which are heavily confusion limited.

Previous searches for HzRSs have been conducted by selecting relatively bright (> 1 mJy) ultrasteep spectrum (USS, $\alpha \geq 1$, $S_\nu \propto \nu^{-\alpha}$) radio sources in shallow surveys covering several thousand square degrees (e.g. S. Rawlings et al. 1996; C. De Breuck et al. 2000; M. J. Jarvis et al. 2001a; A. Saxena et al. 2018a; A. Capetti et al. 2025; L. Ighina et al. 2025), limiting the source discovery space to luminous radio-loud AGNs and quasars, to the extent that very few would be expected (M. J. Jarvis & S. Rawlings 2000; M. J. Jarvis et al. 2001b; M. H. Brookes et al. 2008; L. M. Ker et al. 2012). M. J. Jarvis et al. (2009) dropped the USS requirement, instead cross-matching radio sources which are very faint or not detected in *Spitzer*/Infrared Array Camera (IRAC) or *K*-band imaging, ensuring sources lie at $z > 2$, leading to the discovery of a radio galaxy at $z = 4.88$. More recently, R. Endsley et al. (2022) discovered a radio-loud AGN at $z = 6.8$ by cross-matching deep Very Large Array (VLA) imaging with a sample of Lyman-break galaxy (LBG) candidates, which was later confirmed with ALMA (R. Endsley et al. 2023), demonstrating the strength of cross-matching optical + near-infrared (NIR)-selected high-redshift galaxies with deep radio observations. E. Lambrides et al. (2024) have presented a candidate radio-loud AGN at $z = 7.7$, but this source still requires spectroscopic confirmation.

A population of low-luminosity HzRSs may be relevant in the broader context of recently identified 'Little Red Dots' (LRDs; J. Matthee et al. 2024) discovered with *James Webb Space Telescope* (*JWST*). LRDs are characterized by compact morphologies, distinctive 'V-shaped' spectral energy distributions, and show evidence for AGN activity from broad rest-frame optical emission lines (e.g. J. E. Greene et al. 2024), with the AGN potentially enshrouded by a dense cocoon of gas (e.g. A. Graaff et al. 2025; R. P. Naidu et al. 2025; W. Q. Sun et al. 2026). To date, however, no radio emission associated with accreting SMBHs has been detected from LRDs, including in stacking analyses (H. B. Akins et al. 2025; G. Mazzolari et al. 2025; E. A. Orozco et al. 2025; K. Perger et al. 2025). It therefore remains unclear whether their apparent radio-quiet nature reflects intrinsically weak radio emission compounded by current sensitivity limits, or instead points to alternative power sources, such as extremely compact and dense star-forming regions (J. F. W. Baggen et al. 2024; C. A. Guia, F. Pacucci & D. D. Kocevski 2024). Recent radio observations of a low-redshift ($z = 0.17$) analogue to an LRD with the VLA suggest that at least some of these systems may host radio emission consistent with radio-luminous supernovae (L. F. Rodriguez & I. F. Mirabel 2025). Faint HzRSs could provide complementary insight into high-redshift systems powered by either low-luminosity AGN or intense SF, where the radio emission is detectable (S. Fu et al. 2025).

By utilizing deep radio imaging from the MeerKAT International GHz Tiered Extragalactic Exploration survey Data Release 1 (MIGHTEE DR1; M. Jarvis et al. 2016; C. L. Hale et al. 2025) at 1.3 GHz, together with excellent multiwavelength data, we are able to extend the study of HzRSs to lower-radio powers and larger areas for the first time.

This paper is structured as follows. In Section 2, we present the multiwavelength data and methods used to select the HzRSs. We present the three spectroscopically confirmed HzRSs in Section 3, and compute their SF rates from rest-frame UV, optical, and radio tracers. In Section 4, we explore whether these HzRSs are SF or AGN-dominated, discuss their spectral indices, and compare to expected numbers from the radio luminosity function. Finally, we present our conclusions in Section 5.

All magnitudes reported in this paper are in the AB system (J. B. Oke & J. E. Gunn 1983). We assume a standard cold dark matter cosmology, $H_0 = 70\,\mathrm{km\,s^{-1}\,Mpc^{-3}}$, $\Omega_\mathrm{m} = 0.3$, $\Omega_\Lambda = 0.7$. We use a P. Kroupa (2001) initial mass function (IMF) throughout. For radio spectral indices α, we use the convention $S_\nu \propto \nu^{-\alpha}$ for a source with flux density S_ν at frequency ν. Errors are reported at $1\,\sigma$.

2 DATA AND HZRS SELECTION

In this section we present the multiwavelength data and methods used to select the HzRSs.

2.1 MIGHTEE radio data

The MIGHTEE survey is a MeerKAT (J. L. Jonas 2009) radio survey providing simultaneous continuum (I. Heywood et al. 2022; C. L. Hale et al. 2025), spectral line (I. Heywood et al. 2024), and polarization (A. R. Taylor et al. 2024) data. This work is based on MIGHTEE Data Release 1 continuum data in the COSMOS field at 1.3 GHz, outlined in C. L. Hale et al. (2025). The COSMOS data consist of 22 pointings, with a total on-target time of 139.6 h, covering 4.2 $\mathrm{deg^2}$. Two different versions of the imaging and associated source catalogues are produced, one optimized for sensitivity and one optimized for resolution (see C. L. Hale et al. 2025, for details). In this work, we use the higher-resolution image, which has a circular synthesized beam full width half-maximum of 5.2 arcsec and the measured noise in the centre of the image is 2.4 $\mu\mathrm{Jy\,beam^{-1}}$.

An earlier version of the MIGHTEE radio data, consisting of a single pointing in the COSMOS field (the MIGHTEE Early Science data, see I. Heywood et al. 2022, for details), was cross-matched with deep ground-based optical and NIR imaging (see next section) in I. H. Whittam et al. (2024). We use this Early Science (ES) cross-matched catalogue, together with the deeper DR1 radio catalogue, as the starting point for this work as outlined in the following sections. Due to the wide bandwidth of the

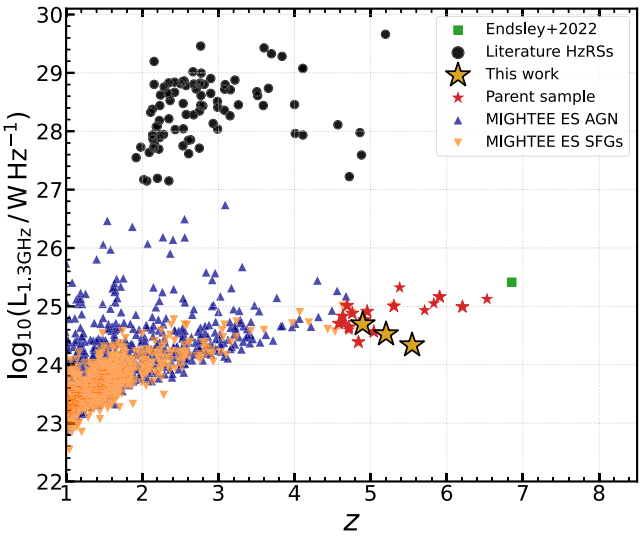

Figure 1. The radio luminosities of the spectroscopically confirmed HzRSs presented in this work, shown by the large gold stars. We show the parent sample which overlaps with COSMOS-3D, determined from cross-matching MIGHTEE radio sources to sources with a photometric redshift $z_{\rm phot} > 4.5$, by the smaller red stars. The blue upward-pointing triangles and orange downward-pointing triangles represent AGNs and SFGs, respectively, from the MIGHTEE Early Science data (MIGHTEE ES; I. H. Whittam et al. 2022). The black circles represent samples from the literature, compiled from C. G. Bornancini et al. (2007), J. J. Bryant et al. (2009), M. J. Jarvis et al. (2009), and A. Saxena et al. (2018a), scaled to 1.3 GHz assuming a spectral index of $\alpha = 0.7$. The green square shows the highest-redshift confirmed radio loud AGN discovered by R. Endsley et al. (2022).

MeerKAT L-band receiver the effective frequency of the MIGHTEE DR1 data varies slightly across the image. We use the effective frequency map released with the DR1 data to scale the radio flux density of each source to 1.3 GHz. Fig. 1 shows the redshift – radio luminosity plane for the star-forming galaxies (SFGs) and AGN from the MIGHTEE ES data (I. H. Whittam et al. 2022) which extends to $z \approx 4.5$.

2.2 Ground-based data

We make use of rest-UV selected catalogues produced by N. J. Adams et al. (2023) in the COSMOS field. The full selection is summarized in their section 2. Deep optical data from the Canada–France–Hawaii–Telescope Legacy Survey (CFHTLS; J.-C. J. Cuillandre et al. 2012) and the Hyper-Suprime Cam Subaru Strategic Program (HSC-SSP; H. Aihara et al. 2019) were combined with NIR data from the UltraVISTA survey (H. J. McCracken et al. 2012), covering around 1.5 deg^2. Sources in this catalogue with $K_s < 25$ were cross-matched to the MIGHTEE ES catalogue using both the likelihood ratio method (K. McAlpine et al. 2012) and visual inspection (I. H. Whittam et al. 2024). Photometric redshifts were determined using both a template-fitting method using LEPHARE (S. Arnouts et al. 1999; O. Ilbert et al. 2006) and machine learning with GPz (I. A. Almosallam et al. 2016a; I. A. Almosallam, M. J. Jarvis & S. J. Roberts 2016b; P. W. Hatfield et al. 2020, 2022). Less than 5 per cent of sources have a photometric redshift in significant disagreement with available spectroscopic redshifts. However, at $z > 4$, spectroscopic redshifts become sparse, and a careful treatment of interloper sources is required. N. J. Adams et al. (2023) go on to select a sample of LBGs at $z \simeq 3.5-5.5$ by using LEPHARE to split the catalogue into galaxies, AGNs and Milky Way stars, mitigating contamination by, for example, ultracool dwarfs (with M, L, and T-type templates from A. J. Burgasser 2014). We make use of their $z = 5$ sample, which contains sources with $4.5 < z_{\rm phot} < 5.5$. We cross-match these LBGs to the host galaxy positions from the I. H. Whittam et al. (2024) MIGHTEE ES cross-matched catalogue.

2.3 *JWST* COSMOS-Web

Since the MIGHTEE catalogues are matched to ground-based imaging, it is entirely possible that highly reddened and intrinsically faint sources will be missed, leading to no ground-based counterpart. We therefore also crossmatch the MIGHTEE catalogue to COSMOS2025 (M. Shuntov et al. 2025). Briefly, this catalogue was constructed by running SEP (K. Barbary 2016), a PYTHON implementation of SOURCE EXTRACTOR (E. Bertin & S. Arnouts 1996), on a χ^2_+ stack of the *JWST* NIRCam *F*115*W*, *F*150*W*, *F*277*W*, and *F*444*W* filters from the 0.54 deg^2 COSMOS-Web survey (C. M. Casey et al. 2023). SOURCEXTRACTOR++ (E. Bertin et al. 2020; M. Kümmel et al. 2020, 2022) is then used to perform multiband model-fitting photometry across all available ground- and space-based imaging. *Hubble F*814*W* imaging (A. M. Koekemoer et al. 2007) is used to reject low-redshift interlopers, while *JWST* Mid-Infrared Instrument (MIRI) *F*770*W* data from COSMOS-Web provide improved stellar mass and dust constraints (e.g. C. Papovich et al. 2023). MIRI imaging covers 0.2 deg^2, such that only a sub-set of the 18 HzRS candidates (Section 2.4) have MIRI coverage. Spectral energy distribution (SED) fitting is then conducted with LEPHARE (S. Arnouts et al. 1999; O. Ilbert et al. 2006), with the outlier fraction compared to spectroscopic samples not exceeding 10 per cent down to $m_{F444W} = 28$. We retain sources with $z_{\rm phot} \geq 4.5$, with this threshold chosen to extend beyond the MIGHTEE ES AGN/SFG separation carried out by I. H. Whittam et al. (2022).

2.4 SED fitting

We use SED fitting to identify robust HzRS candidates and remove low-redshift interlopers from the MIGHTEE-cross-matched sample. Sources from the ground-based catalogue of N. J. Adams et al. (2023) and from COSMOS2025 (M. Shuntov et al. 2025) have already undergone SED fitting analysis using LEPHARE (S. Arnouts et al. 1999; O. Ilbert et al. 2006), with an outlier rate of less than 10 per cent across both studies, when compared to spectroscopic samples. We cross-match the ground-based candidates to the COSMOS2025 catalogue, obtaining consistent model-based photometry from (M. Shuntov et al. 2025) for all available photometry from *JWST*, *Hubble*, Visible and Infrared Survey Telescope for Astronomy (VISTA), and Subaru Hyper Suprime-Cam (HSC). We use BAGPIPES (A. C. Carnall et al. 2018) to verify the photometric redshifts from LEPHARE. We use the non-parametric star formation history (SFH) described by K. G. Iyer et al. (2019) with six lookback time bins and a Dirichlet prior on the lookback times. We place flat priors on the age of the galaxy (100 Myr to the age of the Universe at the redshift), stellar mass (10^6 to 10^{13}M$_\odot$), dust attenuation ($A_V = 0$–4 using the D. Calzetti 1997 law), ionization parameter ($\log U = -4$ to -2), and redshift ($z = 0$–10). Candidate HzRSs are then taken as sources which have agreeing photometric redshifts at $z > 4.5$ from both LEPHARE + BAGPIPES runs. We find no significant

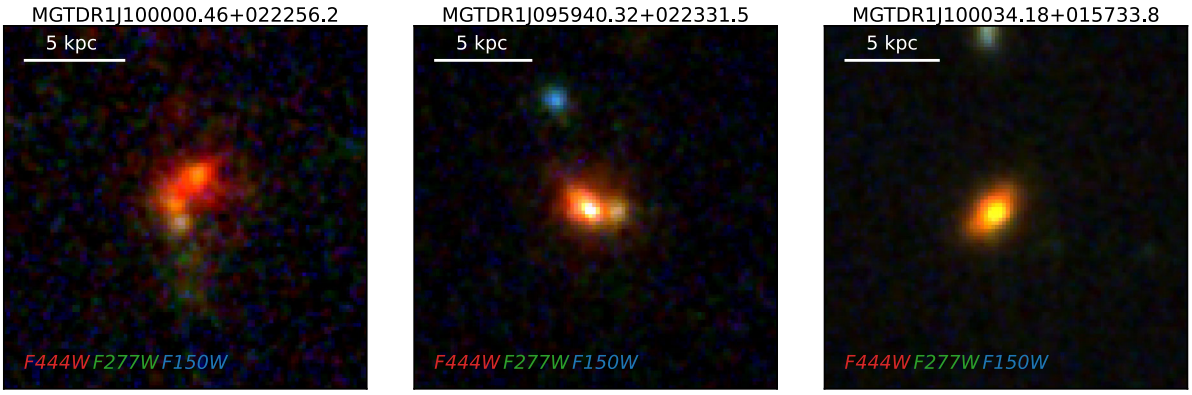

Figure 2. RGB images of the HzRSs presented in this work. The images are 3 × 3 arcsec, and are generated using *F*444*W* (red), *F*277*W* (green), and *F*150*W* (blue). A 5 kpc scale bar is shown for reference. We note that MGT J09594+02233 and MGT J10000+02225 are composed of multiple components, whereas MGT J10003+01573 shows a disc-like morphology with a possible bulge.

differences when the shallower ground-based data is excluded. The SED fitting analysis yields 18 HzRS candidates which overlap with the COSMOS-3D footprint (see Section 2.5). We show their photometric redshifts as a function of their 1.3 GHz luminosities in Fig. 1, alongside HzRSs discovered previously, highlighting the very low radio luminosities we are probing with the new MIGHTEE data compared to previous studies.

2.5 COSMOS-3D

COSMOS-3D is a *JWST* Cycle 3 Large Programme (268h; K. Kakiichi et al. 2024) obtaining NIRCam wide-field slitless spectroscopy (WFSS) in *F*444*W*, covering 0.33 deg^2. The details of the grism extraction are described in R. A. Meyer et al. (2025), Feige et al. (in preparation). WFSS images, 1D and 2D spectra are produced within GRIZLI (G. Brammer 2023). For this, the NIRCam/WFSS data are reduced using GRIZLI[1] version 1.12.11 and JWST pipeline version 1.18, and Calibration References Data System (CRDS) context pmap 1293. Sources from COSMOS2025 with $m_{F444W} < 27.5$ (M. Shuntov et al. 2025) which overlap with the COSMOS-3D footprint are extracted, with this threshold allowing for the detection of faint objects with a single line and no continuum at the sensitivity limit of the grism data. As outlined in the previous section, we find 18 HzRS candidates at $z > 4.5$ which lie in the COSMOS-3D footprint and have $m_{F444W} < 27.5$. We use a script from the DAWN *JWST* Archive (DJA)[2] which measures redshifts by forward-modelling the spectrum with GRIZLI. The cross-dispersion profile was fit with a Gaussian. Continuum and contamination were modelled and subtracted using a flexible 31-knot spline. Emission lines were modelled with Gaussian line profiles assuming a velocity dispersion of 150 km s^{-1}. The fit returned the best-fitting 2D model and redshift solution for Hα within the relevant spectral window. We measure the Hα fluxes from the 1D grism spectrum. The flux density is converted from counts s^{-1} to erg s^{-1} Å^{-1} cm^{-2} using the provided flat-field response. We identify the peak near the redshifted Hα wavelength and integrate over the line pixels. Uncertainties are derived from Monte-Carlo resampling of the spectrum. We retain candidate HzRSs with a signal-to-noise ratio S/N > 2.5 (integrated) for an Hα emission line in agreement with the photometric redshift $z_{\rm phot}$ within 2σ. While this S/N is low in isolation, these detections are evaluated jointly with broad-band SED fitting. This yields three robust HzRSs with the Hα emission line at a redshift in agreement with the photometric redshift. The remaining 15 sources are undetected in the grism spectroscopy. The non-detections are likely related to the SF time-scales probed by Hα and the 1.3 GHz luminosity respectively. This is discussed further in Section 4.1.

We also check the MIRI *F*1000*W* and *F*2100*W* imaging obtained as part of COSMOS-3D. Out of the three HzRSs presented in Section 3, one source is detected in both filters, one in just *F*1000*W*, and the remaining source is not covered by the imaging. We measure fluxes from these images with a flexible Kron aperture using SEP (E. Bertin & S. Arnouts 1996; K. Barbary 2016). To measure the physical properties of the three confirmed HzRSs, we repeat the SED fitting outlined in Section 2.4, but now with a narrow prior of $z_{\rm spec} \pm 0.05$ on the redshift, as determined from the COSMOS-3D WFSS. We present *JWST* RGB images of the HzRSs in Fig. 2, and their COSMOS-3D spectra and SEDs in Fig. 3. The data described here may be obtained from https://doi.org/10.17909/nd3g-1180.

3 RESULTS

We identify three low-luminosity HzRSs at $z > 4.5$. Spectroscopic confirmation has been provided by *JWST* WFSS from the COSMOS-3D survey (K. Kakiichi et al. 2024). Due to the faint nature of these sources, none have a rest-frame optical continuum detection in the grism data. We show the radio luminosities as a function of redshift in Fig. 1 for the parent sample of 18 HzRS candidates (photometric redshifts), and for the three spectroscopically confirmed HzRSs. We show RGB images of the HzRSs in Fig. 2. These sources have radio luminosities $L_{1.3\,\rm GHz} \lesssim 5 \times 10^{24}$ W Hz^{-1} (see Fig. 1), lying at least two orders of magnitude below previously identified HzRSs. This sample represents the first time we are able to probe a regime where the radio emission is potentially dominated by SF, rather than AGN activity, at these redshifts for a sample selected in the radio band. In this section, we present each of the HzRSs, discuss potential low-redshift contamination, describe their morphology and measure their SF rates. In Table 1, we present the

[1] https://grizli.readthedocs.io/
[2] https://dawn-cph.github.io/dja/blog/2025/05/16/simplified_cutout_wfss/

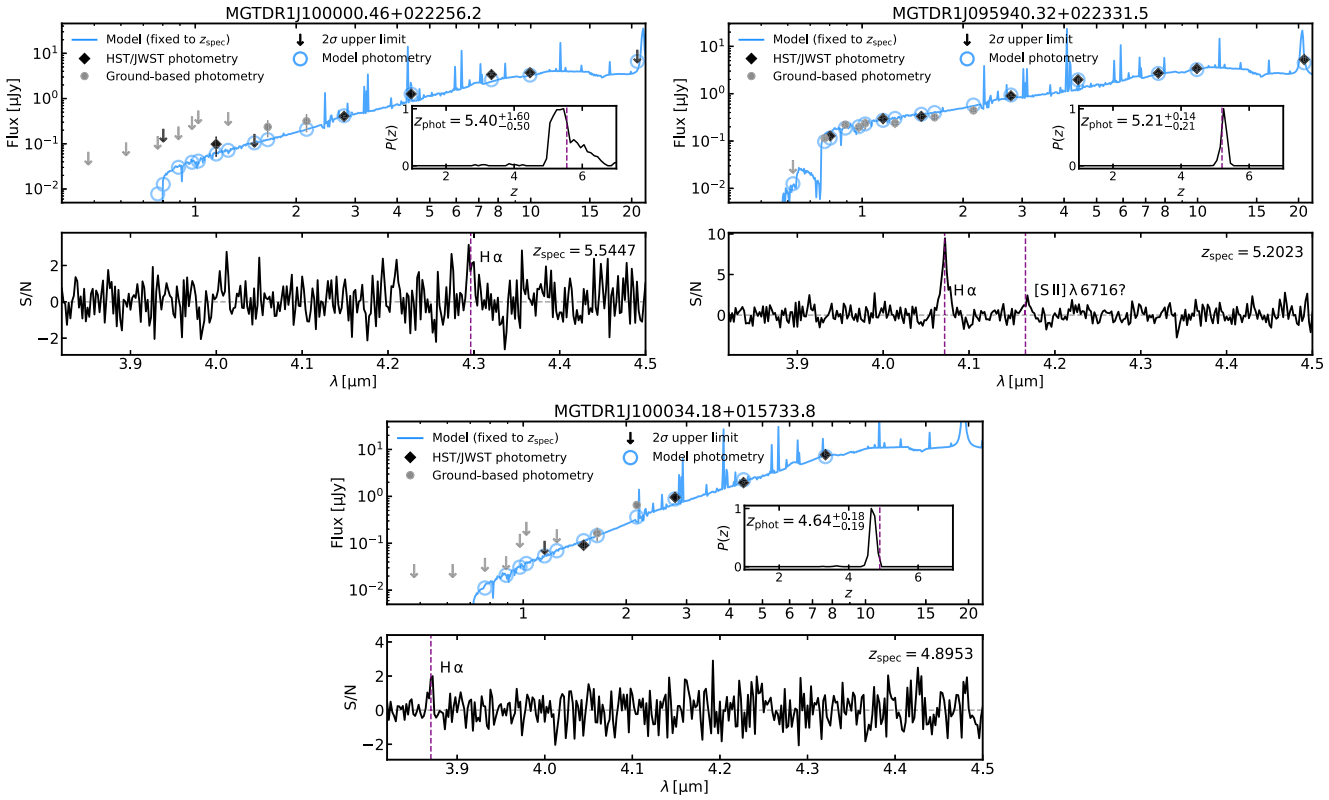

Figure 3. SED fitting (top panels) and *JWST* grism spectroscopy (bottom panels) of the three HzRSs presented in this work. For each source, the top panel shows the best-fitting SED from BAGPIPES when we fix the redshift to z_{spec}. The black diamonds indicate the photometry from *Hubble* F814W, *JWST* NIRCam, and *JWST* MIRI. The grey circles indicate the ground-based photometry from Subaru HSC and VISTA. Non-detections are replaced with arrows indicating $2\,\sigma$ upper limits. Open blue circles indicate the model photometry. The inset panel shows the redshift probability distribution, $P(z)$, when we place a flat prior on the redshift instead of fixing it to z_{spec}. The purple dashed lines in the bottom panels indicate the position of detected emission lines matching the photometric redshift. We also mark the corresponding spectroscopic redshift on the $P(z)$ panel. We find excellent agreement between the photometric redshifts derived from using flat priors and the spectroscopic redshifts measured from the grism spectra for all three sources.

Table 1. Observed spectroscopic, photometric, emission-line, and radio properties of the HzRSs presented in this work, ordered by decreasing spectroscopic redshift. Source IDs are from the MIGHTEE DR1 catalogue. z_{spec} is determined from the H$\,\alpha$ line position in the NIRCam/WFSS data, while z_{phot} is obtained from broad-band SED fitting. $f_{H\,\alpha}$ is the observed H$\,\alpha$ line flux density. $S_{1.3\,GHz}$ and $S_{3\,GHz}$ represent the flux densities at 1.3 GHz from MIGHTEE and 3 GHz from VLA-COSMOS (V. Smolčić et al. 2017) respectively. MGT J09594+02233 and MGT J10000+02225 are undetected in the V. Smolčić et al. catalogue, the 3 GHz flux densities listed for these sources are extracted from the radio image. $L_{1.3\,GHz}$ is the rest-frame radio luminosity computed using the measured spectral index α, while $L^{\alpha=0.7}_{1.3\,GHz}$ assumes a fixed spectral index of $\alpha = 0.7$, both using z_{spec}. Finally, $\alpha^{3\,GHz}_{1.3\,GHz}$ is the spectral index, measured from $S_{1.3\,GHz}$ and $S_{3\,GHz}$.

MIGHTEE DR1 ID	z_{spec}	z_{phot}	$f_{H\,\alpha}$ (10^{-17} erg s^{-1} cm^{-2})	$S_{1.3\,GHz}$ (μJy)	$S_{3\,GHz}$ (μJy)	$L^{\alpha=0.7}_{1.3\,GHz}$ (10^{24} W Hz^{-1})	$L_{1.3\,GHz}$ (10^{24} W Hz^{-1})	$\alpha^{3\,GHz}_{1.3\,GHz}$
MGTDR1 J100000.46+022256.2	5.5447	$5.50^{+1.60}_{-0.50}$	1.03 ± 0.30	11.5 ± 3.5	2.6 ± 2.2	2.16 ± 0.67	13.6 ± 18.4	1.68 ± 0.70
MGTDR1 J095940.32+022331.5	5.2023	$5.21^{+0.14}_{-0.21}$	5.16 ± 0.20	20.1 ± 4.6	8.7 ± 2.1	3.34 ± 0.77	5.36 ± 4.11	0.96 ± 0.40
MGTDR1 J100034.18+015733.8	4.8953	$4.64^{+0.18}_{-0.19}$	2.99 ± 1.13	34.0 ± 4.2	14.2 ± 2.3	4.95 ± 0.61	8.29 ± 3.53	0.99 ± 0.23

redshifts and observable properties of the HzRSs such as their H$\,\alpha$ fluxes, radio flux densities and luminosities, and spectral indices. In Table 2, we present their derived properties, such as dust attenuation, stellar mass, Sérsic fit parameters, and SF rates. Properties derived from SED fitting are measured by fixing to the spectroscopic redshift with a small prior ($\Delta z = \pm 0.05$). In Fig. 3, we show the SED fitting and grism spectroscopy of the HzRSs. In Fig. 4, we show *JWST* NIRCam postage stamp cutouts of the HzRSs, overlaid with MIGHTEE radio contours. For clarity, we use abridged source IDs (MGT J10000+02225, MGT J09594+02233, and MGT J10003+01573) throughout the remainder of the text. The full MIGHTEE DR1 IDs are listed in Table 1.

3.1 MGTDR1 J100000.46+022256.2

MGT J10000+02225 is selected from the COSMOS2025 catalogue (M. Shuntov et al. 2025), and is not detected in the ground-based HSC and VISTA data. SED fitting suggests this source is a massive dusty galaxy with $\log_{10}(M/M_\odot) = 10.72^{+0.21}_{-0.23}$ and $A_V = 2.66^{+0.17}_{-0.18}$. The redshift probability distribution has a broad peak, with $z_{phot} = 5.40^{+1.60}_{-0.50}$, driven by non-detections at $\lambda \lesssim 2\,\mu$m. The

Table 2. Derived physical properties of the HzRSs. Dust attenuation (A_V) and stellar mass are obtained from SED fitting with BAGPIPES . Effective radius R_e and Sérsic index n are taken from Sérsic profile fits in the COSMOS2025 catalogue (M. Shuntov et al. 2025). Star formation rates are inferred independently from SED fitting (averaged over 10 and 100 Myr), dust-corrected Hα emission, and radio luminosity at 1.3 GHz assuming a P. Kroupa (2001) IMF. The SED fitting-derived properties are measured by fixing the redshift to the spectroscopic redshift, with a small prior ($z_{spec} \pm 0.05$).

MIGHTEE DR1 ID	A_V (mag)	$\log_{10}(M/M_\odot)$	R_e (kpc)	n	$SFR^{SED}_{10\,Myr}$ ($M_\odot$ yr^{-1})	$SFR^{H\alpha}$ ($M_\odot$ yr^{-1})	$SFR^{SED}_{100\,Myr}$ ($M_\odot$ yr^{-1})	$SFR^{1.3\,GHz}$ ($M_\odot$ yr^{-1})
MGTDR1 J100000.46+022256.2	$2.66^{+0.17}_{-0.18}$	$10.72^{+0.21}_{-0.23}$	2.11 ± 0.12	1.08 ± 0.12	322^{+161}_{-176}	137 ± 40	154^{+49}_{-37}	226 ± 23
MGTDR1 J095940.32+022331.5	$1.64^{+0.07}_{-0.07}$	$10.16^{+0.11}_{-0.12}$	1.36 ± 0.03	1.66 ± 0.08	300^{+50}_{-46}	273 ± 32	75^{+16}_{-14}	366 ± 36
MGTDR1 J100034.18+015733.8	$3.72^{+0.14}_{-0.21}$	$10.78^{+0.10}_{-0.08}$	0.90 ± 0.01	1.41 ± 0.04	1820^{+244}_{-321}	817 ± 308	386^{+60}_{-72}	569 ± 55

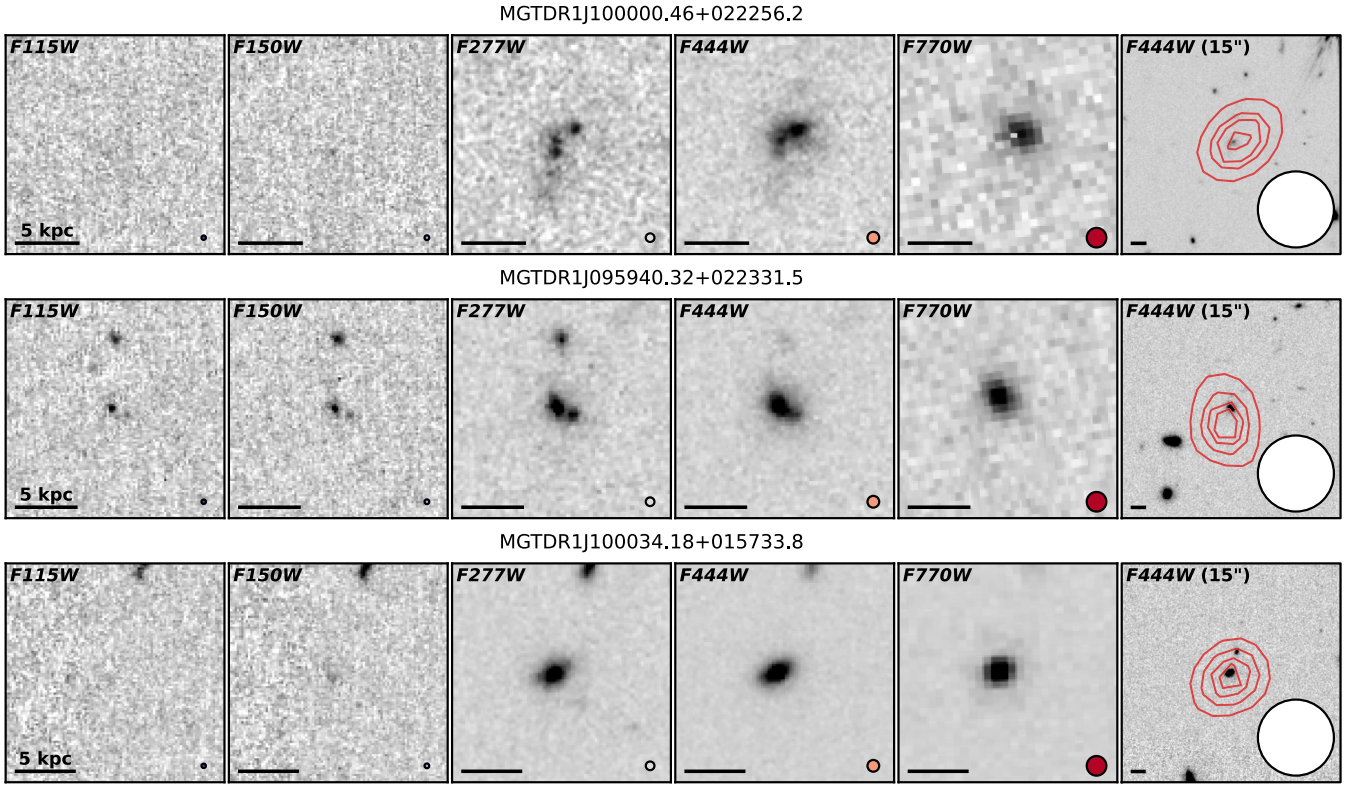

Figure 4. *JWST* NIRCam postage stamp cut-outs of the HzRSs presented in this work. For each source, the first four stamps are 3 × 3 arcsec. The final postage stamp cut-out is 15 × 15 arcsec. In this final cut-out the MIGHTEE continuum contours are overlaid. Contours are drawn at the 90th, 95th, 97.5th, and 99th percentiles, and at the maximum, of the radio cut-out pixel values. The *JWST* images saturate at 2 σ below and 8 σ above the noise level. We show a 5 kpc scale bar in the bottom left, and the *JWST* PSF FWHM and MIGHTEE beam size in the bottom right. Although the radio contours for MGT J09594+02233 appear offset from the NIR position, the offset is 1 arcsec, which is within the uncertainty of the radio centroid at the signal-to-noise ratio of the 1.3 GHz detection.

spectroscopic redshift of $z_{spec} = 5.5447$, assuming the line is Hα, lies within the peak of the redshift probability distribution. MGT J10000+02225 is detected in *F*1000*W*, but lies in a low signal-to-noise region of the *F*2100*W* imaging, so is undetected at 21 μm. This source is also detected with SCUBA-2 at 850 μm (ID S2COS850 78; J. M. Simpson et al. 2019), with $S_{850\,\mu m} = 4.8 \pm 1.0$ mJy. We use this flux to calculate the SFR from the warm dust emission in Section 3.6.

3.2 MGTDR1 J095940.32+022331.5

MGT J09594+02233 is selected from the ground-based LBG sample (N. J. Adams et al. 2023). A deep ground-based optical non-detection with HSC *g* (see Fig. 3) reveals a strong Lyman-break in the original selection. SED fitting finds this source has a stellar mass $\log_{10}(M/M_\odot) = 10.16^{+0.11}_{-0.12}$ with moderate dust attenuation, $A_V = 1.64^{+0.07}_{-0.07}$. This source is detected across all available ground- and space-based filters redwards of 0.7 μm, including *F*1000*W* and *F*2100*W*, providing strong photometric constraints. The photometric redshift of $z_{phot} = 5.21^{+0.14}_{-0.21}$ is in excellent agreement with the spectroscopic redshift of $z_{spec} = 5.2023$. This source has the most robust detection of Hα at 25.8 σ integrated across the line, and there is also a possible detection of [S II] λ 6716. On first inspection, the Hα appears to be broad. We fit a narrow single Gaussian, narrow + broad double Gaussian, and Lorentzian profile to the emission line. At the depth of the COSMOS-3D WFSS, we find no evidence for a preferred narrow + broad profile. Instead, a Lorentzian is moderately preferred over a single Gaussian profile (ΔBIC = 5.7, where BIC is the Bayesian Information Criterion).

3.3 MGTDR1 J100034.18+015733.8

MGT J10003+01573 is selected from the MIGHTEE ES sample, with a photometric redshift $z_{\rm phot} > 4.5$ determined with LEPHARE. SED fitting suggests this source has the largest dust attenuation in the sample with $A_V = 3.72^{+0.14}_{-0.21}$ and a large stellar mass $\log_{10}(M/{\rm M}_\odot) = 10.78^{+0.10}_{-0.08}$. The H α spectroscopic redshift of $z_{\rm spec} = 4.8953$ lies within the peak of the redshift probability distribution. This source is not covered by *F*1000*W* and *F*2100*W* imaging from COSMOS-3D.

3.4 Low-redshift emission line contamination

MGT J10000+02225 and MGT J10003+01573 are highly reddened sources, which prevents robust constraints on the position of the Lyman break and results in non-detections in most ground-based filters. Consequently, their photometric redshift probability distributions are broad and exhibit secondary peaks at $z < 4.5$. Paschen-α (Pa α) emitters at Cosmic Noon (e.g. N. Seymour et al. 2026) are a potential source of contamination. If the detected emission lines in MGT J10000+02225 and MGT J10003+01573 were Pa α ($\lambda_{\rm rest} = 1.875\,\mu$m), the implied redshifts would be $z_{\rm Pa\,\alpha} = 1.29$ and 1.04, respectively. However, there is negligible photometric redshift probability density at $z \approx 1$–1.3 for either source, disfavouring this interpretation. For MGT J10000+02225, the integrated probability below $z = 4.5$ is $P(z < 4.5) = 0.016$, while for MGT J10003+01573 it is $P(z < 4.5) = 0.022$. Other emission-lines (e.g. He I, O I, the Ca II triplet, or the [S III] doublet) are possible at $z \sim 3$–4, but these redshifts contribute only a small fraction of the total $P(z)$. We therefore adopt the high-redshift solutions, identifying the detected lines as H α.

3.5 Morphology

All three HzRSs presented in this work are fit with a Sérsic profile in the NIRCam filters by M. Shuntov et al. (2025). Their effective radii and Sérsic indices are presented in Table 2. All sources have Sérsic indices consistent with a disk ($n \lesssim 1.5$). The effective radii are consistent with size–mass relations at $z \simeq 5$ (e.g. R. G. Varadaraj et al. 2024; N. Allen et al. 2025). They therefore do not have ultracompact morphologies in the rest-frame optical like LRDs, which are generally unresolved (e.g. H. B. Akins et al. 2025). Instead, they are consistent with star-forming galaxies at $z \gtrsim 5$ (e.g. J. S. Kartaltepe et al. 2023).

In addition to the RGB images of the HzRSs in Fig. 2, we also show *JWST* NIRCam and MIRI *F*770*W* postage stamp cut-outs in Fig. 4, along with an overlay of the radio continuum contours. MGT J10000+02225 appears to have an irregular morphology in *F*277*W*, comprised of three distinct clumps possibly surrounded by diffuse emission. MGT J09594+02233 also shows two clumps, with one brighter than the other, in *F*115*W* and *F*150*W*, and consistent with the full width at half-maximum (FWHM) of the point spread function (PSF) in these filters. These could either be due to unobscured AGN emission, or due to compact SF. Compact rest-frame UV morphologies at high redshift can coincide with strong high-ionization lines such as N IV] λ 1486, suggesting either strong compact starbursts or AGN activity (Y. Harikane et al. 2025). The multiple components may also be evidence for ongoing mergers, but confirming this scenario is not possible without follow-up observations which probe the kinematics of the clumps. We discuss further whether these sources are powered by SF or AGN in Section 4.1, but we note that follow-up observations with *JWST*/NIRSpec of rest-frame UV emission lines would provide valuable insight into the nature of these sources. We also note that none of the HzRSs are resolved in the MIGHTEE imaging (see Fig. 4, where the radio contours are consistent with the beam size), which is expected at these redshifts for both SFGs and AGN, and therefore cannot be used to distinguish between the two.

M. Shuntov et al. (2025) also fit bulge + disc profiles to the sources. This fitting is less reliable for MGT J10000+02225 and MGT J09594+02233 due to their irregular, multicomponent morphologies. However, we note that in Fig. 2, it appears that MGT J10003+01573 hosts a bluer bulge and a redder disc. MGT J10003+01573 has a bulge-to-total ratio of 0.15 in *F*277*W* and 0.22 in *F*444*W*. The bulge has a magnitude $m_{F444W} = 24.8$, compared to $m_{F444W} = 23.4$ for the disc. MGT J10003+01573 therefore hosts a faint bulge component, which does not dominate over the total flux, but may host an AGN that contributes some fraction to the total flux. Similarly, we note that neither of MGT J10000+02225 or MGT J09594+02233 are dominated by a point-source component in Fig. 2. We therefore cannot rule out the contribution of an AGN to the appearance of these HzRSs (even for the compact rest-UV morphologies seen for MGT J09594+02233), but conclude that they do not dominate the rest-frame UV and optical emission.

3.6 Star formation tracers

We compute star formation rates (SFRs) based on the radio and H α luminosities, and from SED fitting. We assume that the radio flux is powered entirely by SF. The radio SFR is computed following J. Delhaize et al. (2017), who provide a redshift-dependent calibration

$$\mathrm{SFR}\,[{\rm M}_\odot\,{\rm yr}^{-1}] = f_{\rm IMF}10^{-24}10^{q_{\rm TIR}(z,\alpha)}L_{1.4\,\rm GHz}\,[{\rm W\,Hz}^{-1}] \quad (1)$$

where $f_{\rm IMF} = 1.063$ for a Kroupa IMF (P. Madau & M. Dickinson 2014), $L_{1.4\,\rm GHz}$ is the radio luminosity at 1.4 GHz, and $q_{\rm TIR}$ is the infrared-to-1.4 GHz radio luminosity ratio, which was found to evolve with redshift as $q_{\rm TIR}(z) = (2.88 \pm 0.03)(1+z)^{-0.19\pm0.01}$. We assume a spectral index $\alpha = 0.7$ and correspondingly scale the 1.3 GHz luminosities to 1.4 GHz. We note that whilst we have spectral index measurements for these sources (see Section 3.7), these have very large errors, leading to large errors on the radio luminosity (see Table 1). We therefore fix the spectral index to $\alpha = 0.7$ to provide a direct comparison to other studies which follow the same methodology.

We compute the H α-inferred SFRs following C.-N. Hao et al. (2011), E. J. Murphy et al. (2011), and R. C. Kennicutt & N. J. Evans (2012), which is given by

$$\log_{10}(\mathrm{SFR}/{\rm M}_\odot\,{\rm yr}^{-1}) = \log_{10}(L_{\rm H\,\alpha}/{\rm erg\,s}^{-1}) - 41.27 \quad (2)$$

where $L_{\rm H\,\alpha}$ is the H α luminosity. In order to derive a dust-corrected H α luminosity, we assume that $A_{V,\rm stars} = A_{V,\rm gas}$, i.e. both the stars and emission lines lie within stellar birth clouds, which has been shown to be a reasonable assumption at high redshift (I. Shivaei et al. 2015; R. Smit et al. 2016). We take A_V as measured from the SED fitting. Follow-up observations with *JWST*/NIRSpec would provide measurements of H β, allowing for a dust correction that does not rely on SED fitting.

Finally, the SED-inferred SFR comes from SED fitting with BAGPIPES , as described in Section 2.4, using a non-parametric SF history. We compute SFRs averaged over 10 and 100 Myr

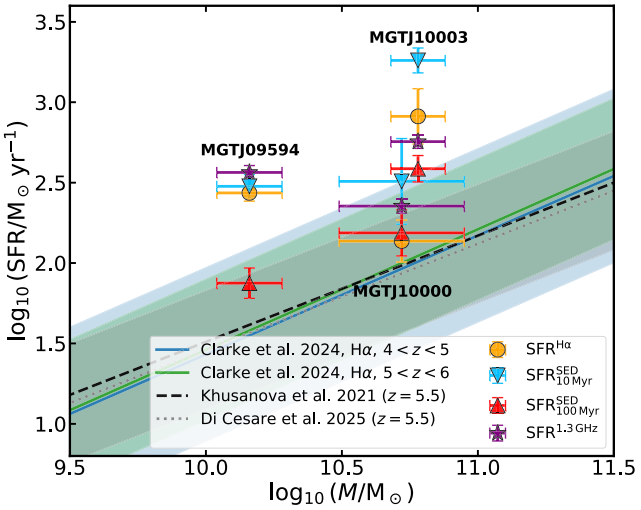

Figure 5. A comparison of the SFRs and stellar masses of the sources presented in this work against the star-forming main sequence at $z \simeq 4-6$, compiled from Y. Khusanova et al. (2021), L. Clarke et al. (2024), and C. Di Cesare et al. (2025) and shown by the dashed, solid, and dotted lines, respectively. The shaded regions indicate the intrinsic scatter. SFRs derived from the Hα flux, SED fitting, and 1.3 GHz radio continuum (assuming Chabrier and Salpeter IMFs) are shown as red circles, blue squares, purple upward triangles, and yellow downward triangles, respectively. Each source is labelled by its abridged ID.

($\mathrm{SFR}^{\mathrm{SED}}_{10\,\mathrm{Myr}}$ and $\mathrm{SFR}^{\mathrm{SED}}_{100\,\mathrm{Myr}}$). This is done to provide two SFR estimates which probe SF time-scales comparable to Hα (~ 10 Myr) and 1.3 GHz luminosity (~ 100 Myr; R. C. Kennicutt & N. J. Evans 2012) We present the SFRs in Table 2. In Fig. 5, we show the positions of the different SF tracers relative to the SF main sequence at $z \simeq 4$–6. We find that $\mathrm{SFR}^{\mathrm{SED}}_{10\,\mathrm{Myr}}$ is in excess of $\mathrm{SFR}^{\mathrm{SED}}_{100\,\mathrm{Myr}}$ for all sources, caused by a recent starburst in the SFH. The SFRs measured from Hα and the 1.3 GHz luminosity are either consistent with, or lie between, the $\mathrm{SFR}^{\mathrm{SED}}$ values. Overall, the SFR values lie on, or up to 1 dex above, the SF main sequence, consistent with star-forming galaxies and starbursts.

We also convert the SCUBA-2 detection at 850 µm for MGT J10000+02225 into a sub-mm derived SFR, following equation (2) from C. L. Carilli & M. S. Yun (1999). This detection probes emission at 130 µm in the rest frame at $z = 5.5447$, tracing the warm dust. Assuming a sub-mm spectral index $\alpha_{\mathrm{sub-mm}} = 3.5$, we find $\mathrm{SFR}^{850\,\mu\mathrm{m}} = 330 \pm 69\,\mathrm{M}_{\odot}\,\mathrm{yr}^{-1}$, consistent with $\mathrm{SFR}^{\mathrm{SED}}_{10\,\mathrm{Myr}}$ and $\mathrm{SFR}^{1.3\,\mathrm{GHz}}$. We note that observations with ALMA would also provide measurements of the warm dust. Correspondingly, we crossmatch the HzRSs presented in this work with A^{3}COSMOS, which is a compilation of public ALMA continuum data in the COSMOS field in bands 3–9 (with large variance in area covered between bands; S. Adscheid et al. 2024). However, we find no counterparts to our HzRSs due to a lack of coverage.

3.7 Radio spectral indices

In Table 1, we present the radio spectral indices of the HzRSs between 1.3 and 3 GHz. MGT J10003+01573 is detected in the V. Smolčić et al. (2017) VLA 3 GHz data and has a radio spectral index $\alpha^{3\,\mathrm{GHz}}_{1.3\,\mathrm{GHz}} = 0.99 \pm 0.23$, indicating that it has a steep spectral shape. The other two sources are undetected in the V. Smolčić et al. catalogue, but we measure their 3-GHz flux densities by extracting pixel values from the radio image. We find MGT J09594+02233 has a radio spectral index $\alpha^{3\,\mathrm{GHz}}_{1.3\,\mathrm{GHz}} = 0.96 \pm 0.40$ and MGT J10000+02225 has $\alpha^{3\,\mathrm{GHz}}_{1.3\,\mathrm{GHz}} = 1.68 \pm 0.70$. Although the resulting spectral index estimates have large uncertainties, it is clear that both sources also have steep spectral shapes. The V. Smolčić et al. (2017) observations lack sensitivity on short baselines meaning that some extended emission may be resolved out, causing an underestimation of the 3-GHz flux densities relative to the measured MIGHTEE flux densities (see C. L. Hale et al. 2023). However, as the three sources in question are all compact, we do not expect this to be contributing to the measured steep spectral shapes. The radio spectral shapes of these sources are discussed further in Section 4.2.

4 DISCUSSION

In this section, we discuss whether the radio emission is powered by SF or AGN activity. We then discuss the impact inverse-Compton scattering may have on our interpretation, and the expected number of radio sources based on the radio luminosity function.

4.1 AGN or star formation?

As shown in Fig. 1, the HzRSs presented in this work straddle a radio luminosity range on the boundary between SFGs and AGNs, as determined by I. H. Whittam et al. (2022). A natural question to ask is whether we can determine whether these sources populate the high-SFR end of the high-redshift galaxy population, or if they are instead powered by low-luminosity AGNs. This requires use of both the rest-frame UV/optical morphology and SED fitting of these sources. In Section 3.5, we found that these sources are likely not dominated by AGNs in the rest-frame UV and optical, based on bulge + disc fitting and their extended, clumpy nature. Instead, we suggested that two of these sources may be undergoing mergers, evidenced by complex multi-component morphologies.

We can also use the results of SED fitting conducted by M. Shuntov et al. (2025), who fit both AGN and galaxy templates to sources in the COSMOS2025 catalogue with LEPHARE. MGT J10003+01573 has a marginally preferred galaxy template, with $\Delta\chi^2(\mathrm{AGN} - \mathrm{galaxy}) = 1.5$. MGT J10000+02225 and MGT J09594+02233 both have a preferred AGN template, with $\Delta\chi^2(\mathrm{galaxy} - \mathrm{AGN}) = 3.5$ and 5.3, respectively. Only MGT J09594+02233 shows moderate preference for an AGN template at $2.3\,\sigma$, while the other two show no significant differences. We note that distinguishing between these templates is limited by a lack of photometry. However, we can again conclude that the SEDs of these sources are not dominated by an AGN.

In Fig. 3, a possible detection of [S II] can be seen for MGT J09594+02233. Assuming the [S II] doublet is blended, we estimate $\log_{10}([\mathrm{S\,II}]/\mathrm{H}\alpha) \sim -1.05$, but we note that the detection of [S II] is marginal, $f_{[\mathrm{S\,II}]} = (4.5 \pm 6.6) \times 10^{-18}\,\mathrm{erg\,s^{-1}\,cm^{-2}}$. This value is consistent with both SFGs and AGNs at high redshift (e.g. J. Scholtz et al. 2025), but without measurements of the [O III]/Hβ ratio it is not possible to study this source further with J. A. Baldwin, M. M. Phillips & R. Terlevich (1981; BPT) diagnostics, used to identify ionisation mechanisms within galaxies and to distinguish SFGs from AGNs.

Next we can compare the SF tracers discussed in Section 3.6. For the purpose of this, we assume that the radio emission is driven entirely by SF when measuring $\mathrm{SFR}^{1.3\,\mathrm{GHz}}$. Additionally, we note that BAGPIPES does not account for AGN emission. We find broad agreement between all SFR tracers, shown in Fig. 5 against the star-forming main sequence at $z = 4$–6. For each source, $\mathrm{SFR}^{\mathrm{SED}}_{10\,\mathrm{Myr}}$ is higher than $\mathrm{SFR}^{\mathrm{SED}}_{100\,\mathrm{Myr}}$, suggesting that these galaxies are undergoing starbursts which are driving the Hα emission. We note that there is large scatter in the measured SFRs. However, the errors shown in Fig. 5 and reported in Table 2 are only the statistical errors which do not account for systematics. Both MGT J10000+02225 and MGT J10003+01573 have limited ground-based photometry, limiting the robustness of SED fitting-derived properties. Their dusty nature results in poor constraints on the SFR from UV tracers, probing time-scales of 100 Myr. Additionally, different assumed SFHs can lead to scatter in the resulting SFR by ~ 1 dex (e.g. S. Tacchella et al. 2022; C. T. Donnan et al. 2026). Our dust correction of the Hα flux is also based on SED fitting, rather than a more reliable Balmer decrement. A related caveat to the lack of a measured Balmer decrement is provided by D. Ismail et al. (2026), who show that Hα-derived SFRs are susceptible to scatter from variations in the optical depth of dust along the line of sight. Our results therefore point broadly to consistent SFRs across the three tracers, with these HzRSs lying on or up to 1 dex above the star-forming main sequence, identifying them as dusty star-forming galaxies. Combining this, the morphology of the sources, and the fact that $\mathrm{SFR}^{\mathrm{SED}}_{10\,\mathrm{Myr}}$ is higher than $\mathrm{SFR}^{\mathrm{SED}}_{100\,\mathrm{Myr}}$, suggests that these galaxies are undergoing a starburst, allowing for the detection of the Hα emission line. The morphology of MGT J09594+02233 and MGT J10000+02225 suggests they are merger-induced starbursts. An AGN contribution cannot be ruled out, but is not likely to dominate over emission from SF.

The interpretation of radio emission from starbursts may also explain the detection rate of Hα. In Section 2.5, we found 18 photometric HzRS candidates which overlapped with the COSMOS-3D footprint, of which three are detected in Hα. Since Hα is sensitive to recent SF on ~ 10 Myr time-scales, whereas GHz radio emission traces SF averaged over ~ 100 Myr, then if the radio emission is SF-driven, only ~ 10 per cent of radio-selected sources are expected to exhibit Hα emission at a given epoch (ignoring dust attenuation and selection effects). This is consistent with our detection rate of $0.17^{+0.12}_{-0.06}$, with binomial errors determined from E. Cameron (2011).

4.2 Radio spectral shapes and inverse-Compton scattering

In Section 3.7, we measured the radio spectral indices of the HzRSs by combining VLA data at 3 GHz (V. Smolčić et al. 2017) with MIGHTEE data at 1.3 GHz. Although the uncertainties on the individual measurements are large as two of the sources are undetected in the 3-GHz catalogue, all three sources exhibit steep ($\alpha \gtrsim 0.7$) radio spectral shapes. The correlation between radio spectral steepness and redshift has been known for several decades (e.g. A. G. G. M. Tielens, G. K. Miley & A. G. Willis 1979) and has motivated the use of ultrasteep-spectrum (USS, $\alpha \gtrsim 1$) selection to identify HzRSs (S. Rawlings et al. 1996; C. De Breuck et al. 2000; M. J. Jarvis et al. 2001a; A. Saxena et al. 2018a; A. Capetti et al. 2025; L. Ighina et al. 2025). Some early interpretations attributed this trend to the dense environments of high-redshift radio galaxies, which may reduce fluid velocities and enhance radiative ageing, leading to steeper synchrotron spectra (e.g. I. J. Klamer et al. 2006). A more comprehensive overview of these scenarios is given by G. Miley & C. De Breuck (2008). However, the main physical mechanism expected to drive steep radio spectra at high redshift is energy loss of relativistic electrons via inverse-Compton (IC) scattering against cosmic microwave background (CMB) photons. While negligible in the local Universe, IC losses become increasingly important at high redshift because the CMB energy density scales as $(1+z)^4$, and are expected to dominate synchrotron losses at $z \gtrsim 3$ (E. J. Murphy 2009). Observational evidence for this effect was provided by I. H. Whittam et al. (2025), who stacked MIGHTEE observations of $\sim 2 \times 10^5$ star-forming Lyman-break galaxies at $z = 3$–5 and showed that, at fixed rest-frame UV magnitude, the flux density and luminosity at 1.4 GHz decline with redshift in agreement with predictions from E. J. Murphy (2009). The steep ($\alpha \gtrsim 0.7$) radio spectra observed for the HzRSs presented in this work can therefore be explained by cooling of relativistic electrons via IC scattering against the CMB, with any potential environmental effects playing a secondary role. If IC losses are affecting the radio emission from these sources, then this would cause the SFRs estimated from the radio emission in this work to be underestimates. Using the estimated $q_{\mathrm{TIR}} \sim 2.4$ at $z = 5$ found by I. H. Whittam et al. (2025) instead of the redshift-dependent J. Delhaize et al. (2017) q_{TIR} relation given in Section 3.6 increases the radio SFRs by a factor of ~ 2. For MGT J10000+02225 and MGT J10003+01573, this would still provide agreement between $\mathrm{SFR}^{1.3\,\mathrm{GHz}}$ and $\mathrm{SFR}^{\mathrm{SED}}_{10\,\mathrm{Myr}}$. While $\mathrm{SFR}^{\mathrm{SED}}_{100\,\mathrm{Myr}}$ probes the SFR on a similar time-scale to the 1.3 GHz luminosity, due to the scatter on the inferred SFRs from SED fitting, we can still conclude that there is no significant radio excess when IC losses are accounted for. MGT J09594+02233 would have $\mathrm{SFR}^{1.3\,\mathrm{GHz}}$ roughly a factor of 2 higher than its largest other SFR measurement, namely $\mathrm{SFR}^{\mathrm{SED}}_{10\,\mathrm{Myr}}$. While this could be interpreted as a radio excess, it is also consistent with a dusty starburst, which may not be well-constrained due to a lack of measurements of the warm dust emission, which reprocesses the UV light. Follow-up observations with ALMA to measure the dust emission would break this degeneracy. Additionally, deeper high-frequency radio data would reduce the uncertainties on the spectral indices and thus confirm this steepening, and this link to IC losses. We also note that determining the relationship between SFR and radio continuum luminosity based on full-SED modelling may also provide slightly lower SFRs than we find using the J. Delhaize et al. (2017) relation. As demonstrated by N. J. Thykkathu et al. (2026), adopting the more recent relation between SFR and radio luminosity from R. H. W. Cook et al. (2024) results in better agreement between the radio-derived and the combined UV + FIR measurements of the cosmic SFR density.

4.3 Expected sources from the radio luminosity function

We are able to determine whether the radio sources we find at these high redshifts are consistent with the current best-fitting radio luminosity function models from deep field data. The two most appropriate luminosity function evolution models at these faint flux densities come from the VLA-3GHz survey of V. Smolčić et al. (2017) and the MIGHTEE survey itself. M. Novak et al. (2017) modelled the evolution in the star-forming galaxy population based on the VLA-3GHz data, constraining the bright-end ($L_{1.4} > 10^{24.5}\,\mathrm{W\,Hz^{-1}}$) of the luminosity function at $z \sim 5$, although it is worth noting that they do not attempt to remove

all AGNs from their sample. Using the evolving luminosity function from M. Novak et al. (2017) we expect to find ~ 20 SFGs in the redshift range $4.85 < z < 5.55$ and at $L_{1.4\,\mathrm{GHz}} > 10^{24}\,\mathrm{W\,Hz^{-1}}$. Similarly, we can use the recent measurement of evolving radio luminosity function from N. J. Thykkathu et al. (2026), who modelled the total radio luminosity function, including contributions from both the AGN and SFG populations, via a statistical approach similar to K. McAlpine, M. J. Jarvis & D. G. Bonfield (2013). From this we can estimate the number of SFGs and AGNs in the area covered by the COSMOS-3D data. Using this, we find that the expected number of SFGs is ~ 12 and the number of AGNs is ~ 2. There are significant uncertainties on these values, due to the fact that most optically invisible sources are either omitted (M. Novak et al. 2017) in measuring the luminosity function, or have to be accounted for statistically (N. J. Thykkathu et al. 2026), and these are likely to be at the higher redshifts ($z > 3$; e.g. F. Gentile et al. 2025). However, they provide a reasonable estimate of the likely relative numbers of SFGs and AGNs. Thus, we would expect to detect far more SFGs than AGNs in these data, and this is consistent with the SFRs determined from both the radio continuum luminosity and other measurements of the SFRs.

5 CONCLUSIONS

In this work, we present three high-redshift radio sources spectroscopically confirmed at $z = 4.9$–5.6 detected in MIGHTEE radio continuum imaging at 1.3 GHz (C. L. Hale et al. 2025). These sources were identified by cross-matching the MIGHTEE DR1 continuum data to ground-based LBG catalogues at $z > 4$ (N. J. Adams et al. 2023) and the COSMOS2025 catalogue (M. Shuntov et al. 2025). These sources were identified as high-redshift candidates through SED fitting of *Hubble F*814*W*, *JWST* NIRCam + MIRI, and ground-based UltraVISTA + Subaru HSC photometry taken from COSMOS2025. The photometric redshifts of these sources were confirmed through a detection of the H$\,\alpha$ emission line in *JWST* COSMOS-3D wide field slitless spectroscopy. The radio luminosities of these sources are at least two orders of magnitude below previously identified HzRSs, with $L_{1.3\,\mathrm{GHz}} \approx 2$–$5 \times 10^{24}\,\mathrm{W\,Hz^{-1}}$. They have steep spectral indices, $\alpha^{3\,\mathrm{GHz}}_{1.3\,\mathrm{GHz}} \approx 0.96$–$1.68$, determined using VLA 3 GHz data (V. Smolčić et al. 2017).

These HzRSs have Sérsic indices and effective radii consistent with the size–mass relations of star-forming galaxies at $z \simeq 5$ (R. G. Varadaraj et al. 2024; N. Allen et al. 2025). None of the sources have a dominant point-source component (as expected for LRDs), indicating that AGNs do not dominate their rest-frame UV and optical flux. Two of the sources, MGTDR1 J100000.46+022256.2 and MGTDR1 J095940.32+022331.5, show complex multicomponent morphologies, which may suggest that they are undergoing mergers. The third source, MGTDR1 J100034.18+015733.8, shows a bulge + disc morphology where the bulge contributes no more than 20 per cent to the total flux.

We compute the SFRs based on SED fitting, H$\,\alpha$, and the 1.3 GHz luminosity, assuming that all of these tracers are powered by SF. The SFRs span ≈ 100–$1800\,\mathrm{M_\odot\,yr^{-1}}$. When averaging the SED-derived SFRs over 10 and 100 Myr, we find that $\mathrm{SFR}^{\mathrm{SED}}_{10\,\mathrm{Myr}}$ is larger than $\mathrm{SFR}^{\mathrm{SED}}_{100\,\mathrm{Myr}}$, caused by a recent starburst in the SFH. The SFRs from H$\,\alpha$ and the 1.3 GHz luminosity are consistent with, or lie between, $\mathrm{SFR}^{\mathrm{SED}}_{10\,\mathrm{Myr}}$ and $\mathrm{SFR}^{\mathrm{SED}}_{100\,\mathrm{Myr}}$ and lie either on or 0.5–1.0 dex above the star-forming main sequence at $z = 4$–6.

The expected number of radio-loud SFGs and AGNs based on the evolving radio luminosity function aligns with the three spectroscopically confirmed sources we find. Additionally, we detect H$\,\alpha$ emission from three out of 18 HzRS photometric candidates which overlap with the COSMOS-3D footprint. This detection rate is broadly consistent with the time-scales probed by H$\,\alpha$ (~ 10 Myr) and the 1.3 GHz luminosity (~ 100 Myr).

We interpret these HzRSs as radio sources which are undergoing starbursts, allowing for the detection of the H$\,\alpha$ emission line. The two HzRSs with complex morphologies may represent merger-triggered starbursts.

The observations presented in this work represent the first detections of SF-powered sources selected via their radio emission at $z > 4.5$, demonstrating the power of combining ultradeep radio continuum surveys in well-studied extragalactic fields with deep ground- and space-based imaging and spectroscopic data sets. Constraining the SF, independent of dust, in some of the earliest galaxies that formed in the Universe is paramount to studying the assembly of the first structures after the big bang, and these observations lay the foundations for future work towards this goal.

ACKNOWLEDGEMENTS

RGV, SF, and MJJ acknowledge support from a UKRI Frontiers Research Grant (EP/X026639/1). AS acknowledges funding from the 'FirstGalaxies' Advanced Grant from the European Research Council (ERC) under the European Union's Horizon 2020 research and innovation programme (Grant agreement No. 789056). IHW, CLH, and MJJ acknowledge support from the Oxford Hintze Centre for Astrophysical Surveys which is funded through generous support from the Hintze Family Charitable Foundation. CLH also acknowledges support from the Science and Technology Facilities Council (STFC) through grant ST/Y000951/1. RAM acknowledges support from the Swiss National Science Foundation (SNSF) through project grant 200020_207349. KK acknowledges support from VILLUM FONDEN (71574) and the Danish National Research Foundation under grant no. 140. JBC acknowledges funding from the *JWST* Arizona/Steward Postdoc in Early galaxies and Reionization (JASPER) Scholar contract at the University of Arizona. ZJL acknowledge the National Key R&D Program of China (MOST) with grant No. 2022YFA1605300, and the National Natural Science Foundation of China (NSFC, grant No. 12273051). This work is based on observations made with the NASA/ESA/CSA *James Webb Space Telescope*. The data were obtained from the Mikulski Archive for Space Telescopes at the Space Telescope Science Institute, which is operated by the Association of Universities for Research in Astronomy, Inc., under NASA contract NAS 5–03127 for *JWST*. These observations are associated with programmes #1727 and #5893.

DATA AVAILABILITY

The MIGHTEE continuum DR1 data used in this work are released with C. L. Hale et al. (2025), the MIGHTEE continuum Early Science cross-matched catalogue is realised with I. H. Whittam et al. (2024), and the MIGHTEE continuum Early Science host galaxy classifications are released with I. H. Whittam et al. (2022). The ground-based galaxy catalogues are released with N. J. Adams et al. (2023). The *JWST* COSMOS-Web data used in this work are released with M. Shuntov et al. (2025).The *JWST*

COSMOS-3D data used in this work may be obtained from https://doi.org/10.17909/nd3g-1180.

REFERENCES

Adams N. J., Bowler R. A. A., Jarvis M. J., Varadaraj R. G., Häußler B., 2023, MNRAS, 523, 327
Adscheid S. et al., 2024, A&A, 685, A1
Aihara H. et al., 2019, PASJ, 71, 114
Akins H. B. et al., 2025, ApJ, 991, 37
Algera H. S. B. et al., 2020, ApJ, 903, 138
Allen N. et al., 2025, A&A, 698, A30
Almosallam I. A., Lindsay S. N., Jarvis M. J., Roberts S. J., 2016a, MNRAS, 455, 2387
Almosallam I. A., Jarvis M. J., Roberts S. J., 2016b, MNRAS, 462, 726
Arnouts S., Cristiani S., Moscardini L., Matarrese S., Lucchin F., Fontana A., Giallongo E., 1999, MNRAS, 310, 540
Baggen J. F. W. et al., 2024, ApJ, 977, L13
Baldwin J. A., Phillips M. M., Terlevich R., 1981, PASP, 93, 5
Barbary K., 2016, J. Open Source Softw., 1, 58
Bertin E., Arnouts S., 1996, A&AS, 117, 393
Bertin E., Schefer M., Apostolakos N., Álvarez-Ayllón A., Dubath P., Kümmel M., 2020, in Pizzo R., Deul E. R., Mol J. D., de Plaa J., Verkouter H. eds, ASP Conf. Ser. Vol. 527, Astronomical Data Analysis Software and Systems XXIX. Astron. Soc. Pac., San Francisco, p. 461
Bornancini C. G., De Breuck C., de Vries W., Croft S., van Breugel W., Röttgering H., Minniti D., 2007, MNRAS, 378, 551
Brammer G., 2023, grizli, Zenodo, doi:10.5281/zenodo.7767790
Brookes M. H., Best P. N., Peacock J. A., Röttgering H. J. A., Dunlop J. S., 2008, MNRAS, 385, 1297
Bryant J. J., Johnston H. M., Broderick J. W., Hunstead R. W., De Breuck C., Gaensler B. M., 2009, MNRAS, 395, 1099
Burgasser A. J., 2014, preprint (arXiv:1406.4887)
Calzetti D., 1997, AJ, 113, 162
Cameron E., 2011, PASA, 28, 128
Capetti A., Balmaverde B., Coloma Puga M., Vizzone B., Jimenez-Gallardo A., García-Pérez A., Venturi G., 2025, A&A, 697, A238
Carilli C. L., Yun M. S., 1999, ApJ, 513, L13
Carnall A. C., McLure R. J., Dunlop J. S., Davé R., 2018, MNRAS, 480, 4379
Casey C. M. et al., 2023, ApJ, 954, 31
Clarke L., Shapley A. E., Sanders R. L., Topping M. W., Brammer G. B., Bento T., Reddy N. A., Kehoe E., 2024, ApJ, 977, 133
Condon J. J., 1992, ARA&A, 30, 575
Cook R. H. W. et al., 2024, MNRAS, 531, 708
Cuillandre J.-C. J. et al., 2012, in Peck A. B., Seaman R. L., Comeron F. eds, Proc. SPIE Conf. Ser. Vol. 8448, Observatory Operations: Strategies, Processes, and Systems IV. SPIE, Bellingham, p. 84480M
De Breuck C., van Breugel W., Röttgering H. J. A., Miley G., 2000, A&AS, 143, 303
de Graaff A. et al., 2025, preprint (arXiv:2511.21820)
Delhaize J. et al., 2017, A&A, 602, A4
Di Cesare C. et al., 2025, A&A, 707, A129
Donnan C. T. et al., 2026, preprint (arXiv:2601.11515)
Dubois Y., Gavazzi R., Peirani S., Silk J., 2013, MNRAS, 433, 3297
Endsley R. et al., 2022, MNRAS, 512, 4248
Endsley R. et al., 2023, MNRAS, 520, 4609
Franco M. et al., 2018, A&A, 620, A152
Fu S. et al., 2025, preprint (arXiv:2512.02096)
Gentile F. et al., 2025, A&A, 697, A46
Greene J. E. et al., 2024, ApJ, 964, 39
Guia C. A., Pacucci F., Kocevski D. D., 2024, RNAAS, 8, 207
Hale C. L. et al., 2023, MNRAS, 520, 2668
Hale C. L. et al., 2025, MNRAS, 536, 2187
Hao C.-N., Kennicutt R. C., Johnson B. D., Calzetti D., Dale D. A., Moustakas J., 2011, ApJ, 741, 124
Harikane Y. et al., 2025, ApJ, 980, 138
Hatfield P. W., Almosallam I. A., Jarvis M. J., Adams N., Bowler R. A. A., Gomes Z., Roberts S. J., Schreiber C., 2020, MNRAS, 498, 5498
Hatfield P. W., Jarvis M. J., Adams N., Bowler R. A. A., Häußler B., Duncan K. J., 2022, MNRAS, 513, 3719
Heywood I. et al., 2022, MNRAS, 509, 2150
Heywood I. et al., 2024, MNRAS, 534, 76
Ighina L. et al., 2025, A&A, 698, A158
Ilbert O. et al., 2006, A&A, 457, 841
Ismail D. et al., 2026, preprint (arXiv:2601.05916)
Iyer K. G., Gawiser E., Faber S. M., Ferguson H. C., Kartaltepe J., Koekemoer A. M., Pacifici C., Somerville R. S., 2019, ApJ, 879, 116
Jarvis M. et al., PoS, MeerKAT2016,6 2016,
Jarvis M. J., Rawlings S., 2000, MNRAS, 319, 121
Jarvis M. J. et al., 2001a, MNRAS, 326, 1563
Jarvis M. J., Rawlings S., Willott C. J., Blundell K. M., Eales S., Lacy M., 2001b, MNRAS, 327, 907
Jarvis M. J., Teimourian H., Simpson C., Smith D. J. B., Rawlings S., Bonfield D., 2009, MNRAS, 398, L83
Jonas J. L., 2009, IEEE Proceedings, 97, 1522
Kakiichi K. et al., 2024, COSMOS-3D: A Legacy Spectroscopic/Imaging Survey of the Early Universe, JWST Proposal. Cycle 3, ID. #5893
Kartaltepe J. S. et al., 2023, ApJ, 946, L15
Kennicutt R. C., Evans N. J., 2012, ARA&A, 50, 531
Ker L. M., Best P. N., Rigby E. E., Röttgering H. J. A., Gendre M. A., 2012, MNRAS, 420, 2644
Khusanova Y. et al., 2021, A&A, 649, A152
Klamer I. J., Ekers R. D., Bryant J. J., Hunstead R. W., Sadler E. M., De Breuck C., 2006, MNRAS, 371, 852
Koekemoer A. M. et al., 2007, ApJS, 172, 196
Kroupa P., 2001, MNRAS, 322, 231
Kümmel M., Bertin E., Schefer M., Apostolakos N., Álvarez-Ayllón A., Dubath P., 2020, in Pizzo R., Deul E. R., Mol J. D., de Plaa J., Verkouter H. eds, ASP Conf. Ser. Vol. 527, Astronomical Data Analysis Software and Systems XXIX. Astron. Soc. Pac., San Francisco, p. 29
Kümmel M., Álvarez-Ayllón A., Bertin E., Dubath P., Gavazzi R., Hartley W., Schefer M., 2022, preprint (arXiv:2212.02428)
Lambrides E. et al., 2024, ApJ, 961, L25
Lapi A. et al., 2011, ApJ, 742, 24
Madau P., Dickinson M., 2014, ARA&A, 52, 415
Matthee J. et al., 2024, ApJ, 963, 129
Mauch T., Sadler E. M., 2007, MNRAS, 375, 931
Mazzolari G. et al., 2025, A&A, 700, A12
McAlpine K., Smith D. J. B., Jarvis M. J., Bonfield D. G., Fleuren S., 2012, MNRAS, 423, 132
McAlpine K., Jarvis M. J., Bonfield D. G., 2013, MNRAS, 436, 1084
McCracken H. J. et al., 2012, A&A, 544, A156
Meyer R. A. et al., 2025, preprint (arXiv:2510.11373)
Miley G., De Breuck C., 2008, A&AR, 15, 67
Muldrew S. I., Hatch N. A., Cooke E. A., 2015, MNRAS, 452, 2528
Murphy E. J., 2009, ApJ, 706, 482
Murphy E. J. et al., 2011, ApJ, 737, 67
Naidu R. P. et al., 2025, preprint (arXiv:2503.16596)
Novak M. et al., 2017, A&A, 602, A5
Oke J. B., Gunn J. E., 1983, ApJ, 266, 713
Orozco E. A., Jiménez-Andrade E. F., Murphy E. J., Smail I., Momjian E., Heywood I., Vega-Gutierrez M., DeCoursey C., 2025, preprint (arXiv:2506.20634)
Overzier R. A., 2016, A&AR, 24, 14
Papovich C. et al., 2023, ApJ, 949, L18
Perger K., Fogasy J., Frey S., Gabányi K. É., 2025, A&A, 693, L2
Rawlings S., Lacy M., Blundell K. M., Eales S. A., Bunker A. J., Garrington S. T., 1996, Nature, 383, 502
Rodriguez L. F., Mirabel I. F., 2025, preprint (arXiv:2512.03331)
Sadler E. M. et al., 2002, MNRAS, 329, 227
Saxena A. et al., 2018a, MNRAS, 475, 5041
Saxena A. et al., 2018b, MNRAS, 480, 2733
Scholtz J. et al., 2025, A&A, 697, A175
Seymour N. et al., 2026,ApJ,998,306,

Shivaei I., Reddy N. A., Steidel C. C., Shapley A. E., 2015, ApJ, 804, 149
Shuntov M. et al., 2025, A&A, 704, A339
Simpson J. M. et al., 2019, ApJ, 880, 43
Smail I., Ivison R. J., Blain A. W., Kneib J.-P., 2002, MNRAS, 331, 495
Smit R., Bouwens R. J., Labbé I., Franx M., Wilkins S. M., Oesch P. A., 2016, ApJ, 833, 254
Smolčić V. et al., 2017, A&A, 602, A1
Sun W. Q. et al., 2026, preprint (arXiv:2601.20929)
Tacchella S. et al., 2022, ApJ, 927, 170
Taylor A. R. et al., 2024, MNRAS, 528, 2511
Thykkathu N. J. et al., 2026, preprint (arXiv:2601.14913)
Tielens A. G. G. M., Miley G. K., Willis A. G., 1979, A&AS, 35, 153
Varadaraj R. G. et al., 2024, MNRAS, 533, 3724
Venemans B. P. et al., 2007, A&A, 461, 823
Whittam I. H. et al., 2022, MNRAS, 516, 245
Whittam I. H. et al., 2024, MNRAS, 527, 3231
Whittam I. H. et al., 2025, MNRAS, 543, 507
Zavala J. A. et al., 2023, ApJ, 943, L9

This paper has been typeset from a TEX/LATEX file prepared by the author.

© The Author(s) 2026.
Published by Oxford University Press on behalf of Royal Astronomical Society. This is an Open Access article distributed under the terms of the Creative Commons Attribution License (https://creativecommons.org/licenses/by/4.0/), which permits unrestricted reuse, distribution, and reproduction in any medium, provided the original work is properly cited.